Bcl6 controls meningeal Th17–B cell interaction in murine neuroinflammation

Maike Hartlehnert[a,1], Anna-Lena Börsch[a,1], Xiaolin Li[a,1], Miriam Burmeister[b,c], Hanna Gerwien[b,c], David Schafflick[a], Michael Heming[a], I-Na Lu[a], Venu Narayanan[a], Jan-Kolja Strecker[a], Anna Kolz[d], Anneli Peters[d,e], Gregory F. Wu[f], Heinz Wiendl[a,c], Lydia Sorokin[b,c], and Gerd Meyer zu Horste[a,2]

[a]Department of Neurology with Institute of Translational Neurology, University Hospital Münster, 48149 Münster, Germany; [b]Institute of Physiological Chemistry and Pathobiochemistry, University of Münster, 48149 Münster, Germany; [c]Cells in Motion Interfaculty Centre, University of Münster, 48149 Münster, Germany; [d]Institute of Clinical Neuroimmunology, University Hospital, Ludwig-Maximilians University Munich, 81377 Munich, Germany; [e]Biomedical Center, Faculty of Medicine, Ludwig-Maximilians University Munich, 81377 Munich, Germany; and [f]Department of Neurology, Washington University in St. Louis, St. Louis, MO 63108

Edited by Lawrence Steinman, Stanford University School of Medicine, Stanford, CA, and approved July 27, 2021 (received for review November 24, 2020)

Ectopic lymphoid tissue containing B cells forms in the meninges at late stages of human multiple sclerosis (MS) and when neuroinflammation is induced by interleukin (IL)-17 producing T helper (Th17) cells in rodents. B cell differentiation and the subsequent release of class-switched immunoglobulins have been speculated to occur in the meninges, but the exact cellular composition and underlying mechanisms of meningeal-dominated inflammation remain unknown. Here, we performed in-depth characterization of meningeal versus parenchymal Th17-induced rodent neuroinflammation. The most pronounced cellular and transcriptional differences between these compartments was the localization of B cells exhibiting a follicular phenotype exclusively to the meninges. Correspondingly, meningeal but not parenchymal Th17 cells acquired a B cell–supporting phenotype and resided in close contact with B cells. This preferential B cell tropism for the meninges and the formation of meningeal ectopic lymphoid tissue was partially dependent on the expression of the transcription factor Bcl6 in Th17 cells that is required in other T cell lineages to induce isotype class switching in B cells. A function of Bcl6 in Th17 cells was only detected in vivo and was reflected by the induction of B cell–supporting cytokines, the appearance of follicular B cells in the meninges, and of immunoglobulin class switching in the cerebrospinal fluid. We thus identify the induction of a B cell–supporting meningeal microenvironment by Bcl6 in Th17 cells as a mechanism controlling compartment specificity in neuroinflammation.

single-cell RNA-seq | CNS meninges | Th17 | Bcl6 | ectopic lymphoid tissue

Multiple sclerosis (MS) is a chronic autoimmune demyelinating disorder of the central nervous system (CNS) with complex etiology (1, 2). The relative contribution of T and B cells to neuroinflammation may be location specific. In fact, T cells are abundant in MS lesions in the CNS parenchyma (3), while B cells are enriched in border tissues surrounding the CNS of MS patients (4). These border tissues include the multilayered fibrous membranes termed meninges that ensheath the CNS together with the protective cerebrospinal fluid (CSF) (5). Both the meninges and CSF serve immune-related functions with likely contribution to diseases (6). In MS, class-switched and affinity-matured immunoglobulins (Ig) and late B lineage cells accumulate in the CSF (7, 8), and B cell–rich ectopic lymphoid tissue can develop in the meninges in chronic MS (4, 9) with a gradient of neuronal damage originating from the meninges (10, 11). However, immunological mechanisms controlling meningeal inflammation are poorly understood.

Experimental autoimmune encephalomyelitis (EAE) in rodents replicates many aspects of human MS (12). Especially, the EAE model induced by adoptive transfer (AT) of myelin-specific interleukin (IL)-17 producing T helper (Th17) cells (13) represents a good model to study meningeal pathology, because it triggers robust inflammation and accumulation of ectopic lymphoid tissue in the meninges (14). Similar to human MS, parenchymal infiltrates in EAE consist mainly of T cells, while meningeal inflammation has a strong B cell component (15). Features of neuroinflammation are, thus, site-specific in the parenchyma versus meninges and can be modeled in rodents. This compartmentalization has not been well characterized, and the mechanisms of meningeal T/B cell interactions are unknown.

We previously identified the transcription factor Bcl6 in $CD4^+$ T cells as a promising candidate to control meningeal T/B cell interaction because it enables T cells to promote B cell maturation and class switching (16) and exacerbates two variants of EAE (17). However, Bcl6 controls the T follicular helper (TFH) cell lineage (16) by repressing competing Th cell lineages (18), and Bcl6 does not affect the in vitro differentiation of Th17 cells (17, 19, 20)—the Th cell lineage that induces EAE. This in vitro versus in vivo discrepancy led us to speculate that Bcl6 may preferentially modulate Th17 cell functions in vivo such as their interaction with B cells.

Significance

The meninges protect the central nervous system but also host lymphocytes in neuroinflammation. In human multiple sclerosis, preferentially B cells accumulate in the meninges. By generating a compartment-specific transcriptional map of meningeal versus parenchymal leukocytes in experimental neuroinflammation, we found a follicular phenotype of meningeal B cells and a corresponding follicular helper-like phenotype in meningeal Th17 cells. The meninges thus instructed a site-specific local phenotype to proinflammatory autoreactive T cells. We identified the transcription factor Bcl6 in Th17 cells to promote interactions with meningeal B cells, isotype-switching, and B cell-supporting chemokines. This may describe a mechanism controlling meningeal autoimmunity and helps understanding how the meninges, as a recently recognized immunologically active site, contribute to autoimmune tissue damage in multiple sclerosis.

Author contributions: A.P., H.W., and G.M.z.H. designed research; M. Hartlehnert, A.-L.B., X.L., M.B., H.G., D.S., V.N., and A.K. performed research; J.-K.S., G.F.W., and L.S. contributed new reagents/analytic tools; M. Hartlehnert, A.-L.B., X.L., M. Heming, and I.-N.L. analyzed data; and M. Hartlehnert, L.S., and G.M.z.H. wrote the paper.

Competing interest statement: A patent application covering the method for reconstructing T cell receptor information from 3′ libraries has been applied with the title "Circulation Method to Sequence Immune Repertoires of Individual Cells" under the filing no. LU101949 by X. L. and G.M.z.H. (date of filing: July 29, 2020).

This article is a PNAS Direct Submission.

[1]M. Hartlehnert, A.-L.B., and X.L contributed equally to this work.

[2]To whom correspondence may be addressed. Email: gerd.meyerzuhoerste@ukmuenster.de.

This article contains supporting information online at https://www.pnas.org/lookup/suppl/doi:10.1073/pnas.2023174118/-/DCSupplemental.

Published September 3, 2021.

We here performed in-depth characterization of meningeal versus parenchymal leukocytes at the single-cell level in the spinal cord (SC) of Th17 cell-induced EAE. We found evidence of ongoing Th17/B cell interaction in the meninges while B cells remained excluded from the parenchyma. By reconstructing clonality information, we found that antigen-specific Th17 cells adopted site-specific transcriptional states that differed between the meninges and parenchyma. This was at least partially controlled by Bcl6 in Th17 cells, which was required for the induction of a B cell–supporting and lymphoid-tissue inducing microenvironment in the meninges and CSF, likely signaling through stromal cells. This identifies noncanonical effects of Bcl6 in the Th17 lineage controlling the site-specific B cell–dominated meningeal inflammation.

Results

High-Resolution Characterization of SC Inflammation in Th17-Mediated EAE. We initially aimed to deeply characterize the prominent meningeal inflammation (14) occurring in EAE induced by adoptive transfer of T cell receptor (TCR)-transgenic myelin-reactive $2D2^{tg}$ Th17 donor cells ($V\beta11^+$) (AT-EAE) (21) (Fig. 1*A*). We used intravenous (iv) injection of fluorophore-labeled CD45 antibody to distinguish $CD45^{high}CD45iv^{neg}$ tissue-resident leukocytes (TRL) from endovascular leukocytes as described (22, 23) and applied this to the SC parenchyma and meninges (*SI Appendix*, Fig. S1).

We first generated single-cell transcriptomes of TRL sorted from SC meninges (4,068 cells) and parenchyma (4,071 cells) of C57BL/6 recipients of $2D2^{tg}$ Th17 donor cells at peak of AT-EAE (named wild-type [wt] recipients [=wt-R]; Dataset S1). In unbiased cell-type clustering of the combined single-cell RNA-sequencing (scRNA-seq) dataset, we identified 24 individual clusters (*Materials and Methods* and Fig. 1*B*) and annotated them based on highly expressed genes (Dataset S2) and predefined marker gene sets (*SI Appendix*, Fig. S2 *A–C*). We identified two clusters of B lineage cells (Bc) (*Cd79a*, *Ms4a1*/CD20, *Cd74*/MHC class II chain) with either a more-naïve (Bc; *Ighd*) or a more-differentiated phenotype (diffBc; $Cd19^{low}$) (Fig. 1*B* and *SI Appendix*, Fig. S2 *A–C*). We identified eight $CD4^+$ T cell (*Cd3e*, $Cd8a^{neg}$) clusters that spanned a wide spectrum of phenotypes (Fig. 1*B*). Of these, three clusters expressed the *Il17a*, *Rorc* markers of Th17 cells, two expressed the *Foxp3*, *Il2ra*/CD25 regulatory T cell markers, and three expressed markers of proliferation (proli; *Mki67*/Ki67, *Cdk1*) (Fig. 1*B* and Dataset S2). The identification of cytotoxic (cyto) and myeloid lineage cells was in accordance with expectations from previous studies of the brain meninges and in other EAE models (23, 24) (Fig. 1*B* and *SI Appendix*, Fig. S2 *A–D*). We, thus, successfully characterized leukocytes from the inflamed SC parenchyma and meninges.

The Transcriptional Phenotype of Infiltrating Lymphocytes Depends on the Microenvironment. We next combined the scRNA-seq data from all $CD4^+$ T cell clusters and compared the gene expression between meninges and parenchyma (Dataset S3). Differentially expressed (DE) genes between compartments were related to T cell trafficking (*Ccr7*, *Cxcr4* up, *Ccl1*, *Ccl4*, *Cxcr6* down) in the meninges. In addition, genes related to TFH cell function (*Icos*, *Il21r*, *Cxcr4*, *Stat3*) were up-regulated in the meninges. Conversely, $CD4^+$ T cells in parenchyma increased expression of Th17-related genes (*Il17a*, *Rorc*) with some signs of Th1 differentiation and pathogenicity (*Irf1*, *Ifng*, *Tnf*) (*SI Appendix*, Fig. S3*A*). Differential expression analysis of the combined Th17 clusters (Dataset S4), rather than combined $CD4^+$ T cells, revealed similar cell trafficking gene patterns in the meninges (*Cxcr4* up, *Ccr2*, *Cxcr6*, *Itgb7* down) (*SI Appendix*, Fig. S3*B*) and down-regulation of Th17-related (*Il17a*, *Rorc*) and Th1-related transcripts (*Il12rb1*, *Stat1*, *Irf1*, *Tnf*) in the meninges (*SI Appendix*, Fig. S3*B*). Merged Th17 gene scores also differed between compartments (*SI Appendix*, Fig. S3*C* and Dataset S5).

Bulk RNA-seq of $V\beta11^+$ cells sorted from both SC compartments identified that the donor-derived $CD4^+$ T cells also down-regulated Th17-related (*Ctsw*, *Ikzf1* down, *Crem* up) and Th1-related transcripts (*Tnf*, *Socs1*) in the meninges (*SI Appendix*, Fig. S3*D* and Dataset S6). The tissue microenvironment thus shapes the compartment-specific phenotype of encephalitogenic Th17 cells, with acquisition of a TFH-like phenotype in the meninges and signs of Th1 transdifferentiation in the parenchyma. More generally, this suggests zonation of autoimmune mechanisms between CNS compartments.

We next tracked donor-derived Th17 cells in our scRNA-seq dataset by identifying their defined $2D2^{tg}$ TCR expression (*SI Appendix*, *Supplementary Methods* and Fig. S3*E*) (25). Such $2D2^{tg}$ cells were more prevalent in the parenchyma (*SI Appendix*, Fig. S3 *F–I*). In both the meninges and parenchyma, $2D2^{tg}$ cells were enriched in clusters identified as activated and proliferating $CD4^+$ T cell and Th17 clusters (*SI Appendix*, Fig. S3*I* and Dataset S7). Subclustering of these clusters by tissue of origin was impossible due to the low total cell numbers. Genes indicating proliferation (*Mki67*, *Top2a*) and activation (*Cd28*) were induced in 2D2 compared to non-2D2 $CD4^+$ T cell clusters (Dataset S8). This indicates increased activation and proliferation of myelin-specific Th17 cells.

Myelin-Reactive Th17 Cells Preferentially Induce Meningeal but Not Parenchymal B Cell Infiltration in the SC. We next systematically compared the cellular composition between the meninges (wt-R-men) and the parenchyma (wt-R-par). We initially classified clusters into B cell (Bc, green), $CD4^+$ T cell (CD4, orange), cytotoxic (cyto, blue), and myeloid cell (gray) lineages (Fig. 1 *B* and *C* and *SI Appendix*, Fig. S2*D*). Already in this broad classification, B cells predominated in the meninges (29% meningeal versus 1% parenchymal TRL). Conversely, $CD4^+$ T cells were more prevalent in the parenchyma (CD4: 46% parenchymal versus 29% meningeal TRL), while myeloid cells were comparably represented in both compartments (Fig. 1*C* and Datasets S9 and S24). Testing for compositional differences using all 24 clusters confirmed the predominance of B cells in the meninges and of multiple $CD4^+$ T cell and cytotoxic clusters in the parenchyma (Fig. 1*D*). Two clusters classified as Th17 cells (Th17-1, proliTh17) were more abundant in the parenchyma, while the Th17-2 cluster was more abundant in the meninges.

To confirm these results, we performed flow cytometry of meninges versus parenchyma-derived leukocytes at the peak of AT-EAE. We found that B cells were 9.2-fold more abundant in the meninges than the parenchyma, while $CD4^+$ T cells were 1.8-fold higher in the parenchyma (Fig. 1*E* and Dataset S10). The proportion of $V\beta11^+2D2^{tg}$ donor-derived cells of all leukocytes and of all $CD4^+$ T cells was higher in the parenchyma (Fig. 1*E*) in accordance with the TCR tracking data (*SI Appendix*, Fig. S3*H*). The most pronounced cellular differences between the meninges versus parenchyma thus involve B cells and Th17/$CD4^+$ T cells.

We next morphologically localized cell types using semiquantitative cellular heatmaps of SC cross-sections with attached meninges (*Materials and Methods*). We measured the number ($CD3^+$, $V\beta11^+CD3^+$) or area ($B220^+$, $F4/80^+$) occupied by cells and related this to the cross-sectional area, which was smaller in the meninges (Fig. 1*F*). When comparing the resulting cellular density ($CD3^+$, $V\beta11^+CD3^+$; cells/mm^2) or proportion of area infiltrated ($B220^+$, $F4/80^+$; %) between the meninges and the parenchyma, $B220^+$ B cells were almost exclusively restricted to the meninges (Fig. 1*G*), and the densities of $CD3^+$ T cells and $V\beta11^+2D2^{tg}$ donor T cells were significantly higher in the meninges (Fig. 1*G* and Dataset S11), while there was no difference in the area occupied by $F4/80^+$ macrophages. Flow cytometry and immunofluorescence microscopy generated slightly different results since histological

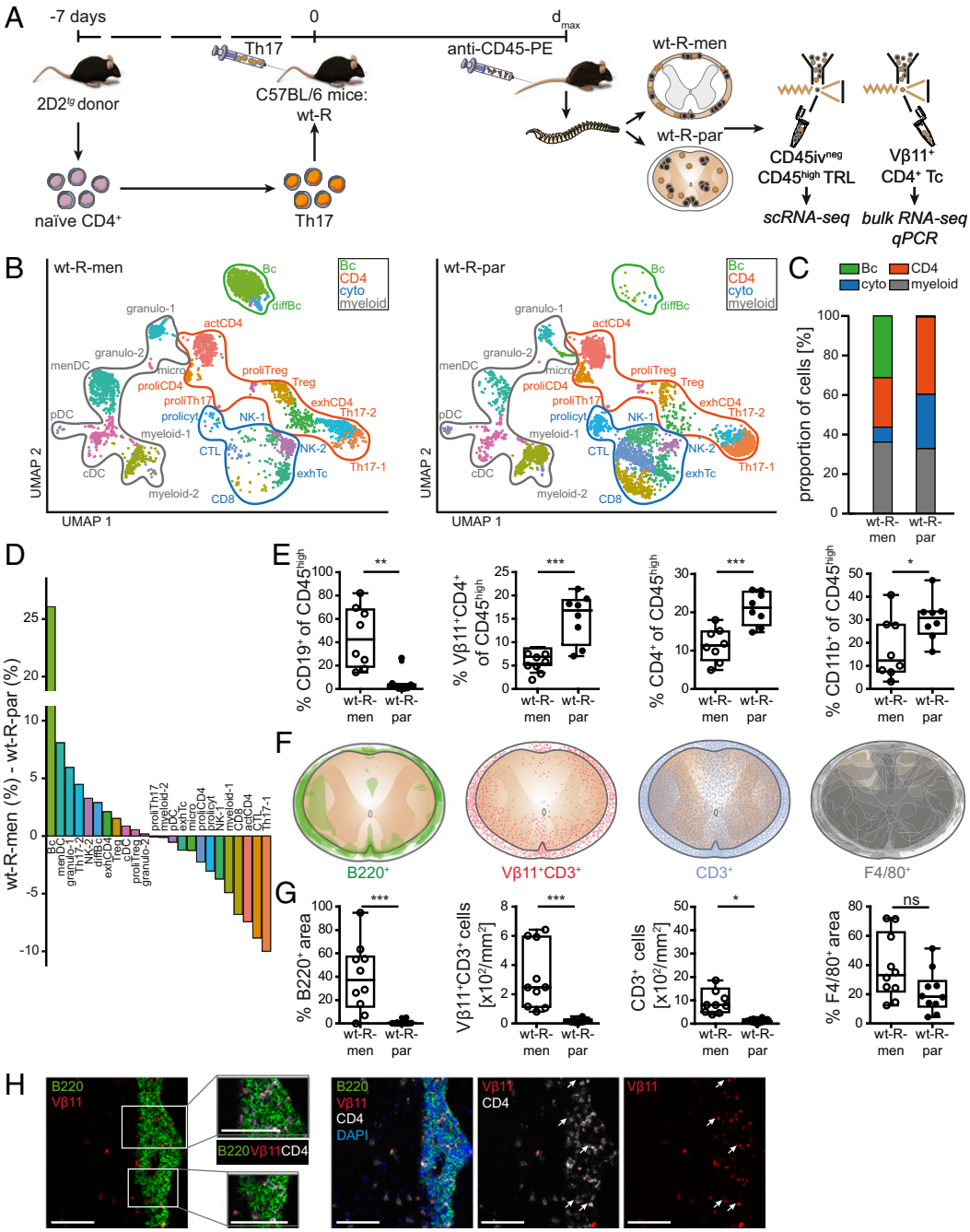

Fig. 1. Myelin-reactive Th17 cells preferentially induce meningeal B cell infiltration in the SC. (*A*) Schematic: CD44^{low}CD62L^{high}CD4$^+$ T cells (violet) sorted from 2D2^{tg} donor mice were differentiated in vitro (orange) with TGF-β1/IL-6 and IL-23 (13). These were iv injected into C57BL/6 recipient mice (wt-R) to induce AT-EAE. At maximum disease severity of AT-EAE, phycoerythrin (PE)-labeled anti-CD45 antibody (3 μg/mouse) was iv injected, and leukocytes were isolated from the SC meninges (men; *Top*) and parenchyma (par; *Bottom*). CD45iv^{neg}CD45^{high} cells were defined as TRL and sorted for scRNA-seq; Vβ11$^+$CD4$^+$CD45iv^{neg} T cells (Tc) were sorted for bulk RNA-seq and qPCR (*SI Appendix*, Fig. S1). (*B*) Single-cell transcriptomes from TRL isolated from SC meninges (men; 4,068 cells; *Left*) and parenchyma (par; 4,071 cells; *Right*) from five wt-R (*A*) depicted in Uniform Manifold Approximation and Projection plots and annotated manually (*SI Appendix*, Fig. S2). Clusters classified as B cells (Bc; green; Bc, diffBc), CD4$^+$ T cells (CD4; orange; actCD4, proliCD4, proliTreg, Treg, exhCD4, Th17-1, Th17-2, proliTh17), CD8$^+$ T and natural killer cells (cyto; blue; CD8, CTL, prolicyt, exhTc, NK-1, NK-2), and myeloid cells (myeloid; gray; pDC, granulo-1, granulo-2, cDC, menDC, micro, myeloid-1, myeloid-2). (*C*) Stacked bar plot of cell-type proportions classified in *B*. (*D*) Differences of cluster proportions in men versus par. Positive values indicate higher abundance in men. (*E*) Proportions of indicated cell types were quantified by flow cytometry of viable TRL in men (open) and par (closed). Gating in *SI Appendix*, Fig. S1. (*F*) PFA-fixed frozen cross-sections were stained by immunofluorescence (IF). The area occupied by B220$^+$ (*Left*) and F4/80$^+$ cells (*Right*), and the number of Vβ11$^+$CD3$^+$ and CD3$^+$ cells (*Middle*) were quantified manually. Heatmaps represent overlays of $n = 10$ mice of lumbar SC sections. (*G*) Quantification of % area occupied by B220$^+$ (*Left*) and F4/80$^+$ cells (*Right*), or the density of Vβ11$^+$CD3$^+$ and CD3$^+$ cells (*Middle*) as in *F*. Each dot represents the mean of three SC sections (cervical, thoracic, lumbar) per mouse. Median, 25th to 75th percentiles, and 1.5-fold interquartile range indicated in *E* and *G*. (*H*) Representative IF (two sections per wt-R, three wt-R) of SC longitudinal section of a recipient mouse at peak of disease. (Scale bars, 100 μm.) Compare with *SI Appendix*, Fig. S4 *A* and *B*. (diff)Bc, (differentiated) B cells; CD4, CD4$^+$; T cells, (Tc); act, activated; Th17, Th17 cells; Treg, regulatory Tc; proli, proliferating; exh, exhausted; CD8, CD8$^+$ Tc; CTL, cytotoxic T lymphocytes; NK, natural killer cells; prolicyt, proliferating cytotoxic Tc; granulo, granulocytes; micro, microglia; (men/p/c)DC, (meningeal/plasmacytoid/classical) dendritic cells; myeloid, myeloid cells. Student's *t* test was used for normally distributed datasets, otherwise Mann–Whitney *U* test. $^*P < 0.05$, $^{**}P < 0.01$, $^{***}P < 0.001$; ns, not significant.

analyses quantified cell densities (Fig. 1*G*), whereas flow cytometry measured the proportion of total $CD45^{high}$ leukocytes (Fig. 1*E*).

Immunofluorescence confocal microscopy of the SC meninges confirmed colocalization of $V\beta11^+$ T cells with $B220^+$ B cells (Fig. 1*H* and *SI Appendix*, Fig. S4 *A* and *B*). We also found a significant correlation between the density of $V\beta11^+$ and $B220^+$ cells ($r = 0.62$, $R^2 = 0.38$, $P = 0.03$) in the meninges but not in the parenchyma ($r = 0.23$, $R^2 = 0.02$, $P = 0.27$; *SI Appendix*, Fig. S4*C*). There was no correlation between $V\beta11^+$ and $F4/80^+$ cell densities in either the meninges ($r = 0.42$, $R^2 = 0.18$, $P = 0.11$) or parenchyma ($r = 0.28$, $R^2 = 0.17$, $P = 0.22$, *SI Appendix*, Fig. S4*D*). Hence, while $V\beta11^+2D2^{tg}$ cells represent a higher proportion of the total $CD45^{high}$ infiltrate in the parenchyma, they occur at a higher density in the meninges in close association with $B220^+$ B cells that exhibit specific tropism for the meninges.

Bcl6 Controls Th17 Effector Function Only In Vivo in a Compartment-Specific Manner. We next identified the transcription factor Bcl6 as a promising candidate in T cells to control meningeal Th17/B cell interaction because it generally enables T cells to promote B cell class switching (16), is up-regulated in Th17 cells upon transfer into the CNS (14), and exacerbates two variants of EAE (*SI Appendix*, Fig. S5 *A* and *B*) (17). In addition, in the bulk RNA-seq data from $V\beta11^+CD4^+$ T cells sorted from the SC meninges and parenchyma of wt-R at peak of AT-EAE, *Bcl6* was expressed at a higher level than in the differentiated Th17 cells pretransfer (Fig. 2*A*), and this was confirmed by qPCR (Fig. 2*B*). *Bcl6* was already up-regulated in $V\beta11^+CD4^+$ T cells sorted from draining inguinal lymph nodes in the early phase of AT-EAE (Fig. 2*B*).

To test the functional role of Bcl6 in meningeal neuroinflammation, we used $CD4^{Cre}Bcl6^{fl/fl}2D2^{tg}$ (Bcl6KO) mice to delete Bcl6 from myelin-reactive $2D2^{tg}$ T cells. Th17 differentiation from naïve $CD4^+$ T cells was unaffected by Bcl6 deletion (*SI Appendix*, Fig. S5*C*) as described previously (17, 19, 20). Bulk RNA-seq of Th17-differentiated $V\beta11^+CD4^+$ T cells collected before transfer also revealed no significantly DE genes between Bcl6KO and wt cells (Dataset S12). Bcl6 is known to promote EAE after in vivo transfer (17). To resolve the discrepancy between unchanged Th17 cell differentiation in vitro and Bcl6 promoting Th17 cell function after in vivo transfer (17), we postulated that Bcl6 would only affect differentiation when Th17 cells are restimulated with antigen.

To address this experimentally, we restimulated T cells extracted from draining lymph nodes and spleen of $MOG_{35–55}$-immunized mice in the presence of $MOG_{35–55}$ antigen and under Th17-polarizing conditions and found reduced IL17A-production in Bcl6KO mice compared to wt controls (Fig. 2*C*), while T cell proliferation was not reduced in Bcl6KO (*SI Appendix*, Fig. S5*D*).

To better characterize this "in vivo-restricted" function, we performed scRNA-seq of TRL sorted from the SC meninges (3,650 cells) and parenchyma (4,279 cells) of recipient mice at peak of EAE after transfer of Bcl6KO-derived $2D2^{tg}$ Th17 cells (Fig. 2 *D* and *E* and *SI Appendix*, Fig. S5*E* and Dataset S2). We first compared the meningeal leukocyte composition between Bcl6KO recipients (named Bcl6KO-R) and wt-R and found a strong decrease in the B cell, Th17 cell (Th17-1, Th17-2), and granulo-1 clusters in Bcl6KO-R (Fig. 2 *D* and *E*). Conversely, the proportion of several myeloid clusters as well as the Treg and multiple cytotoxic clusters increased in the meninges of Bcl6KO-R compared to wt-R (Fig. 2 *D* and *E* and *SI Appendix*, Fig. S5 *F*, *J*, and *K* and Datasets S9 and S25). We then compared the parenchymal TRL composition between genotypes and found that the proportion of clusters classified as $CD4^+$ T cells, especially activated and proliferating $CD4^+$ T cell clusters (actCD4, proliCD4), was reduced in Bcl6KO-R compared to wt-R (19% versus 46%) (*SI Appendix*, Fig. S5 *F–H* and Datasets S9 and S26). Similarly, the Th17 cell clusters (Th17-1, Th17-2, proliTh17) were reduced, while the Treg cluster doubled in Bcl6KO-R compared to wt-R parenchyma (5% versus 2%, Dataset S9). Inversely, cytotoxic leukocyte clusters and plasmacytoid and classical dendritic cell (pDC/cDC) clusters increased in the Bcl6KO-R parenchyma (*SI Appendix*, Fig. S5 *F–H*). Bcl6 expression in Th17 cells, thus, promoted Th17/B cell–dominated inflammation in the meninges and $CD4^+$ T cell–dominated inflammation in the parenchyma.

Using flow cytometry, we confirmed that the meninges of Bcl6KO-R contained lower proportions of $B220^+$ B cells and $V\beta11^+$ T cells than wt-R (Fig. 2*F* and Dataset S13). The proportion of $V\beta11^+$ T cells in the parenchyma was also lower in Bcl6KO-R compared to wt-R (*SI Appendix*, Fig. S5*L* and Dataset S14). Cellular density ($CD3^+$, $V\beta11^+CD3^+$; cells/mm^2) or proportion of area infiltrated ($B220^+$; %) defined by immunofluorescence microscopy confirmed a smaller $B220^+$ B cell infiltrate and less dense $V\beta11^+2D2^{tg}$ donor T cell infiltration in the meninges of Bcl6KO-R compared to wt-R. Total $CD3^+$ T cell density was reduced in Bcl6KO-R in both meninges and parenchyma (Fig. 2*G* and *SI Appendix*, Fig. S5 *K–M* and Dataset S11). Bcl6 expression in Th17 cells, thus, promoted the occurrence of meningeal B cells.

Bcl6 in Th17 Cells Promotes Their Lymphoid Tissue-Inducing Phenotype in the SC Meninges. We next aimed to understand how Bcl6 in Th17 cells controlled these compartment-specific cellular changes. For highest transcriptome coverage, we performed bulk RNA-seq of $V\beta11^+CD4^+$ T cells sorted from the meninges and parenchyma of Bcl6KO-R and wt-R. In total, 130 transcripts DE between genotypes were coregulated in both compartments, 143 transcripts were only DE in the parenchyma, and 636 transcripts were specifically DE in the meninges indicating partially site-specific effects of Bcl6 in Th17 cells (*SI Appendix*, Fig. S6*A* and Dataset S15).

Notably, only in the meninges, $V\beta11^+$Bcl6KO $CD4^+$ T cells lost expression of transcripts promoting lymphoid tissue formation (*Lta*/Lymphotoxin-α, *Ltb*, *Il17f*) and B cell maturation (*Il21*) (Fig. 2*H* and Dataset S16). We confirmed down-regulation of *Lta* and *Il17a* in sorted $V\beta11^+CD4^+$ T cells by qPCR (Fig. 2*I*). In genotype-specific scRNA-seq data, lymphoid tissue-inducing transcripts (*Lta*, *Ltb*, *Il17a*) were also down-regulated in Bcl6KO-R-men versus wt-R-men, and this down-regulation preferentially occurred in Th17 clusters (Fig. 2*J* and *SI Appendix*, Figs. S6*B* and S7 and Dataset S25). This suggests that Bcl6 drives a lymphoid tissue-inducing phenotype in Th17 cells specifically in the meninges.

In the parenchyma, $V\beta11^+$Bcl6KO $CD4^+$ T cells instead gained expression of Th1-related transcripts (*Eomes*, *SI Appendix*, Fig. S6*C*). In both compartments, $V\beta11^+$Bcl6KO $CD4^+$ T cells gained expression of Treg-related transcripts (*Foxp3*, *Smad7*), suggesting that Bcl6 represses differentiation to competing Th cell lineages in a site-specific fashion.

Bcl6 in Th17 Cells Is Required for the Generation of Follicular Meningeal B Cells. We next characterized how Bcl6 deficiency in donor Th17 cells affected the phenotype of meningeal B cells in neuroinflammation. We merged all B cell clusters in the scRNA-seq dataset and restricted this analysis to the meninges as parenchymal B cells were scarce.

In the meninges, Bcl6KO-R–derived B cells up-regulated transcripts related to antigen presentation (*H2-DMa*, *H2-DMb2*, *H2-Ab1)* (Fig. 3*A* and Dataset S17) and down-regulated transcripts previously identified in meningeal follicular B cells (FOBc) in B cell–dependent EAE (26) (*Hspa1a*/HSP70-1A, *Hspa1b*/HSP70-1B) and are described to regulate immune responses to myelin antigen (27).

To achieve higher resolution, we next subclustered all meningeal Bc transcriptomes into five subclusters (Fig. 3*B* and *SI Appendix*, Fig. S6*D* and Dataset S18). When comparing genotypes, two subclusters annotated as Bc-1 and FOBc were markedly reduced in Bcl6KO-R meninges (Fig. 3*C*), and both expressed the known FOBc marker *Fcer2a*/CD23 (28, 29) (Fig. 3*D* and Dataset S19). Cluster Bc-1 additionally expressed genes associated with

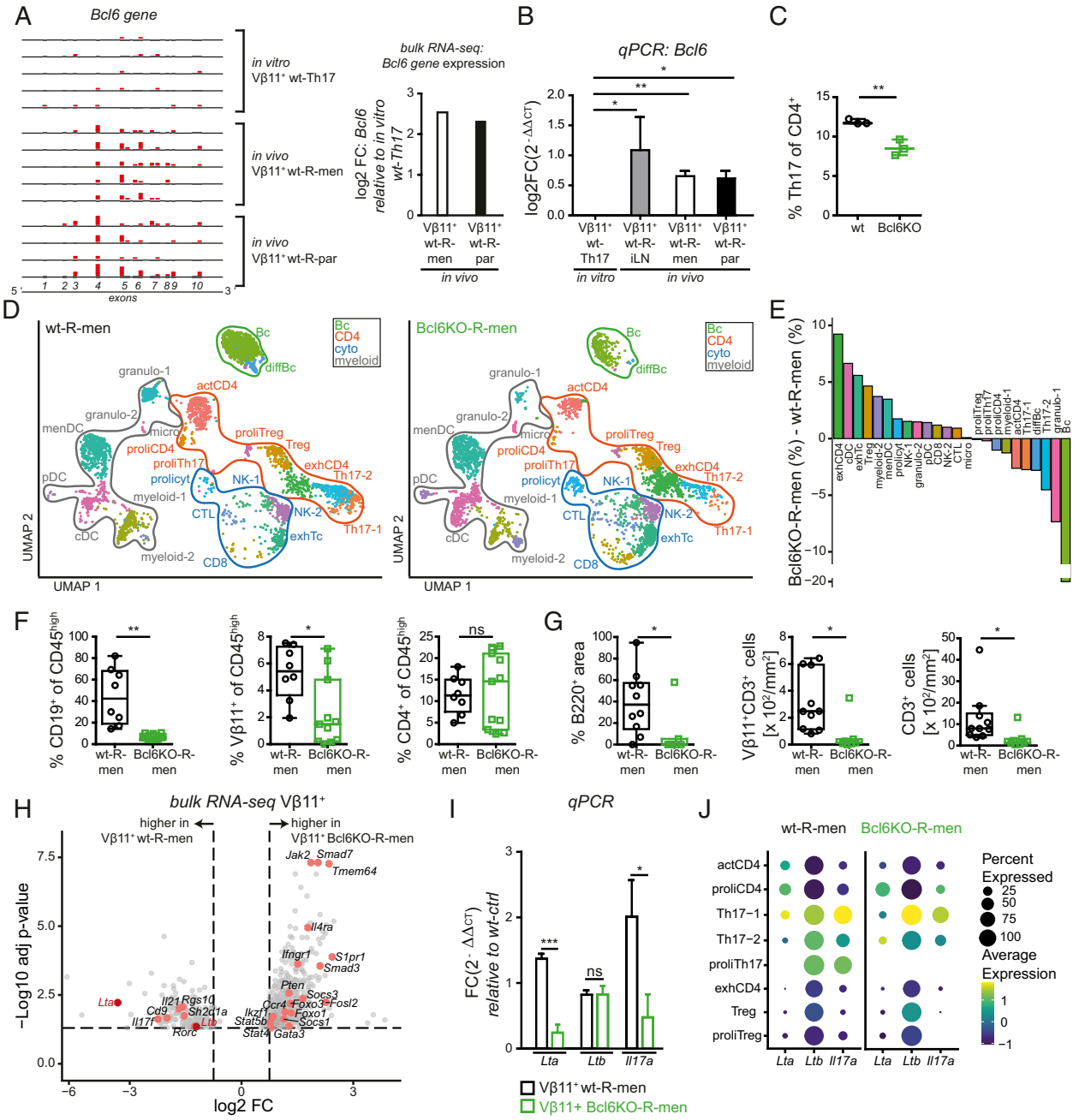

Fig. 2. Bcl6 controls local Th17 effector functions in a microenvironment-specific manner. (*A*) C57BL/6 recipient mice (wt-R) were iv injected with Th17 cells from wt 2D2^{tg} donors (Fig. 1*A*). Bulk RNA-seq was performed on in vitro differentiated Th17 cells (Vβ11$^+$ wt-Th17) and on in vivo Vβ11$^+$CD4$^+$ T cells sorted (*SI Appendix*, Fig. S1) from SC meninges (men) and parenchyma (par) of wt-R. Raw reads aligned to the *Bcl6* gene (*Left*) and log2 fold change (FC) of *Bcl6* gene expression between in vitro Vβ11$^+$ Th17 cells and Vβ11$^+$ cells from men or par (*Right*) are depicted (Datasets S6 and S12). (*B*) qPCR of *Bcl6* in in vitro differentiated Vβ11$^+$ Th17 cells or in wt-R derived in vivo Vβ11$^+$CD4$^+$ T cells sorted from inguinal lymph nodes (iLN) on day 6 after transfer or from the men or par at peak of AT-EAE. (*C*) Wt or CD4^{Cre}Bcl6$^{fl/fl}$ (Bcl6KO) mice were immunized with MOG$_{35–55}$, and after 10 d, CD4$^+$ T cells were isolated from iLN and spleen and cultured under Th17 polarizing conditions; intracellular IL-17A was measured by flow cytometry after 4 h of restimulation. Dots represent biological replicates. (*D*) CD45iv^{neg}CD45^{high} TRL extracted from SC men of five wt-R (*Left*) and five recipients of CD4^{Cre}Bcl6$^{fl/fl}$2D2^{tg} donor cells (Bcl6KO-R, *Right*) were subjected to scRNA-seq (*SI Appendix*, Fig. S5*E*). Transcriptomes of wt-R-men (4,068 cells) and Bcl6KO-R-men (3,650 cells) depicted in Uniform Manifold Approximation and Projection plots. Clusters as in Fig. 1*B*. (*E*) Bar plots showing differences of cluster proportions in Bcl6KO-R-men versus wt-R-men. Positive values indicate higher abundance in Bcl6KO-R-men. (*F*) Proportions of indicated cell types quantified by flow cytometry of TRL in the meninges of wt-R (black) and Bcl6KO-R (green). Gating as in Fig. 1*E* and *SI Appendix*, Fig. S1. (*G*) The proportion of area occupied by B220$^+$ (*Left*) and the density of Vβ11$^+$CD3$^+$ (*Middle*) and CD3$^+$ cells (*Right*) were quantified in cervical, thoracic, and lumbar SC sections (*SI Appendix*, Fig. S5*I*). Each dot depicts the mean from three SC sections (cervical, thoracic, lumbar) per mouse. Median, 25th to 75th percentiles, and 1.5-fold interquartile range indicated in *F* and *G*. (*H*) Donor-derived Vβ11$^+$CD4$^+$CD45iv^{neg}CD45^{high} cells sorted from the SC meninges of wt-R and Bcl6KO-R were processed by bulk RNA-seq as in *A* (*SI Appendix*, Fig. S5*E*). Volcano plot of genes DE between genotypes in men. Thresholds: –Log10 adjusted *P* value < 0.05, log2FC > 0.75. (Dataset S16) (*I*) qPCR of *Lta*, *Ltb*, and *Il17a* in sorted Vβ11$^+$CD4$^+$CD45iv^{neg}CD45^{high} cells from Bcl6KO-R-men versus wt-R-men. (*J*) Dot plot depicting selected genes in clusters identified as CD4$^+$ T cells in scRNA-seq dataset in wt-R-men and Bcl6KO-R-men. Student's *t* test used for normally distributed datasets, otherwise Mann–Whitney *U* test. *$P < 0.05$, **$P < 0.01$, ***$P < 0.001$; ns, not significant.

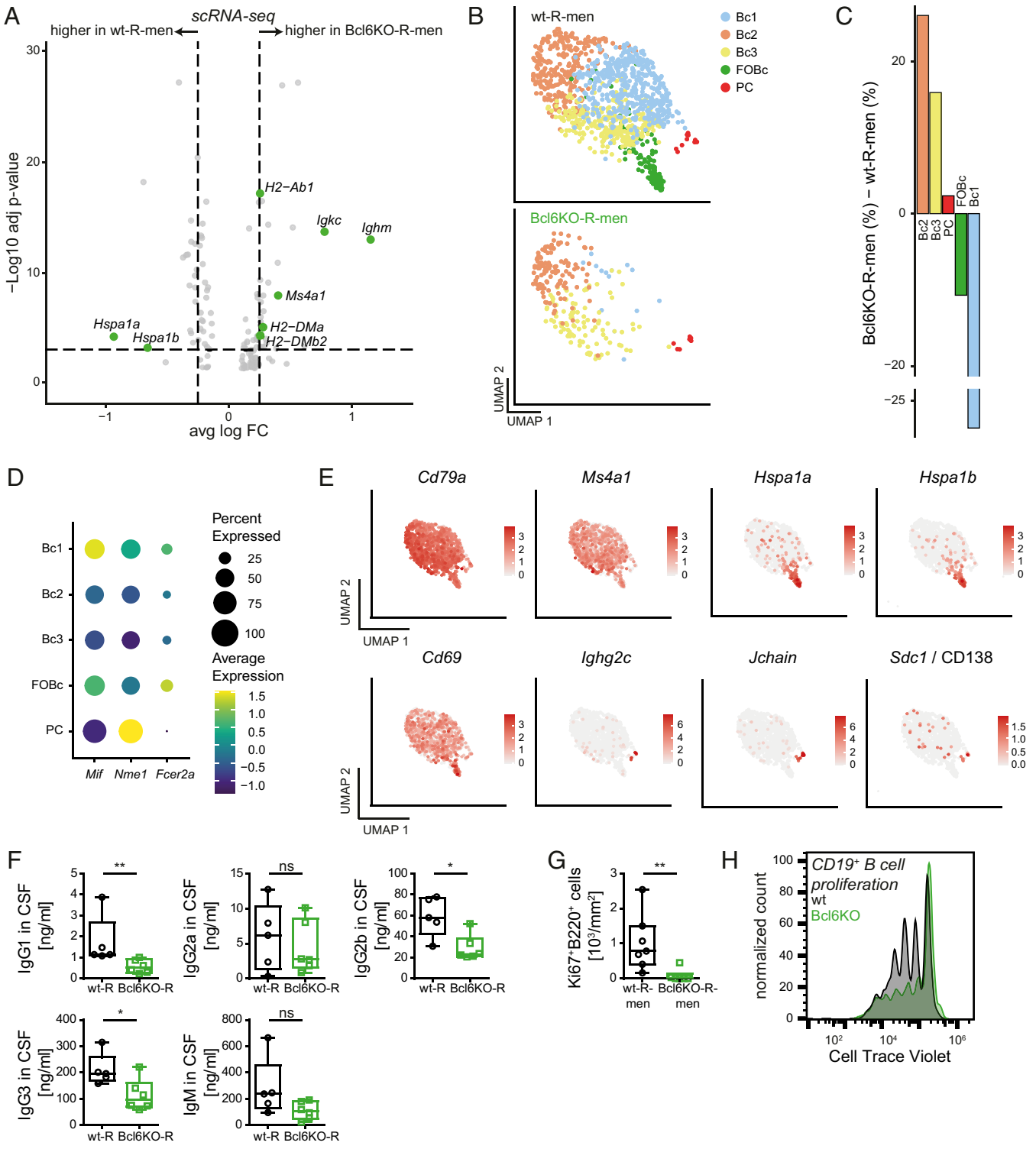

Fig. 3. Bcl6 in Th17 cells influences the development of follicular B cells in the meninges. (*A*) Transcriptomes identified as B cells (Bc and differentiated [diff] Bc clusters) in meninges (men) were merged; volcano plot depicts DE genes between genotypes. Thresholds: −Log10 adjusted *P* value < 0.001, average logFC > 0.25 (Dataset S17). (*B*) Bc transcriptomes as in *A* subclustered into wt-R-men and Bcl6KO-R-men–derived cells. FOBc, follicular Bc; PC, plasma cells. (*C*) Bar plot showing differences of Bc subcluster proportions in the men of Bcl6KO-R versus wt-R. Positive values indicate higher abundance in Bcl6KO-R-men. (*D*) Dot plot of selected genes in Bc subclusters merged from wt-R-men and Bcl6KO-R-men. (*E*) Feature plots of selected Bc markers genes. (*F*) CSF was collected from the cisterna magna of wt-R and Bcl6KO-R at peak of AT-EAE, and concentrations of Ig isotypes were quantified. Differentially abundant isotypes (Dataset S20) are depicted. (*G*) The density of Ki67^{+}B220^{+} cells was quantified in lumbar SC sections in wt-R-men versus Bcl6KO-R-men. Dots represent biological replicates. Box-whisker dot plots (median/25th to 75th percentiles/1.5-fold interquartile range) in *F* and *G*. (*H*) In vitro differentiated Th17 cells from 2D2^{tg} (wt) or CD4^{Cre}Bcl6$^{fl/fl}$2D2^{tg} (Bcl6KO) donor mice were cocultured with labeled (CellTrace Violet) MOG$_{35–55}$-specific B cells from secondary lymphoid organs of a naïve TH mouse in a 1:2 ratio and in the presence of MOG$_{35–55}$. B cell proliferation was analyzed after 3 d with flow cytometry. **P* < 0.05, ***P* < 0.01; ns, not significant.

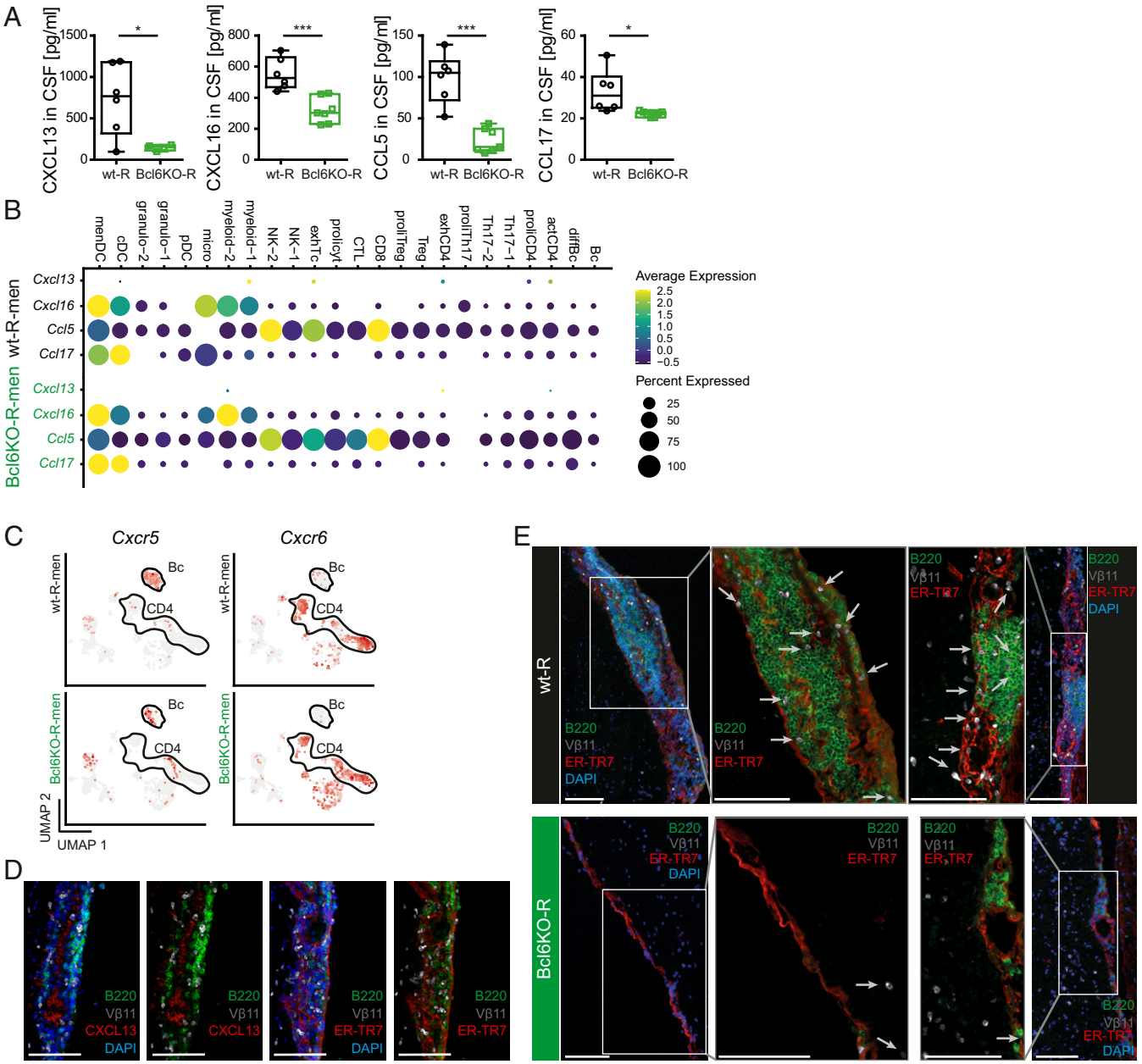

Fig. 4. Bcl6 in Th17 cells promotes meningeal lymphoid tissue formation in neuroinflammation. (*A*) CSF was collected from the cisterna magna of wt-R and Bcl6KO-R at peak of AT-EAE. The concentration of the chemokines shown (Dataset S22) was quantified. Concentrations of differentially abundant chemokines are shown (median/25th to 75th percentiles/1.5-fold interquartile range). (*B*) Dot plot depicting the gene expression of differentially abundant chemokines from *A* in all scRNA-seq clusters defined in Fig. 1*B* in the meninges (men) of wt-R and Bcl6KO-R. (*C*) Feature plots of selected chemokine receptors in wt-R-men and Bcl6KO-R-men. (*D*) Representative immunofluorescence staining (IF) of SC longitudinal sections of meningeal B cell follicles in a representative wt-R at peak AT-EAE stained for the indicated markers. (Scale bars, 100 μm; one representative of staining of three mice.) (*E*) Representative IF of SC longitudinal sections of representative wt-R and Bcl6KO-R at peak AT-EAE stained for the indicated markers. (Scale bars, 100 μm; one representative of stainings of three to five mice.) FRC is fibroblastic reticular cells. Student's *t* test used for normally distributed datasets, otherwise Mann–Whitney *U* test. $*P < 0.05$, $***P < 0.001$.

high transcriptomic activity (e.g., *Ncl*, *Eif2f2*, *Eif4a1*), suggesting activation, and *Mif* (Fig. 3*D*), a transcript with relevance in B cells in MS (30, 31). Cluster FOBc expressed markers of activated FOBc (*Hspa1a*, *Hspa1b*, and *Cd69)* (26) (Fig. 3 *B–E* and Dataset S18). Other B cell clusters decreased (Fig. 3*C*) but were still detectable in Bcl6KO-R meninges. The smallest B cell subcluster resembled class-switched plasma cells (PC; *Ighg2c*, *Xbp1*, *Sdc1*/CD138, *Mki67*/Ki67, *Nme1*; Fig. 3 *B–E*).

We next tested whether Bcl6 in Th17 cells also affected isotype class switching. Therefore, we collected CSF from the cisterna magna of wt-R versus Bcl6KO-R mice at peak of AT-EAE and quantified antibody isotypes with an enzyme-linked immunosorbent assay (ELISA)-based proteomics assay. The concentration of IgG1, IgG2b, and IgG3 was lower in the CSF from Bcl6KO-R compared to wt-R (Fig. 3*F* and Dataset S20). This suggests that Bcl6 in Th17 cells promotes class switching to isotypes IgG1, IgG2b, and IgG3 in accordance with class-switching effects of Th17 cells reported previously (32). Due to low sample volume, we were unable to normalize for total protein content. In accordance with isotype proteins, the *Ighg1* and *Ighg2b* expression in our

scRNA-seq dataset was also reduced in meningeal B cells from Bcl6KO-R compared to wt-R (*SI Appendix*, Fig. S6*E*). To investigate the effect of Bcl6KO in Th17 cells on meningeal B cell proliferation, we histologically quantified the density of $Ki67^{+}B220^{+}$ B cells in the meninges and found a significant reduction in Bcl6KO-R (Fig. 3*G* and Dataset S21). In accordance, in vitro differentiated Bcl6KO Th17 cells promoted the in vitro proliferation of MOG-specific B cells at lower efficiency than wt Th17 cells (Fig. 3*H*). This suggests that the autoimmunity-associated follicular phenotype and subsequent class switching and proliferation of meningeal B cells are at least partially controlled by Th17 cells in a Bcl6-dependent manner.

Bcl6 Induces the Ability to Coinitiate a Local Inflammatory Feed-Forward Loop in Meningeal Th17 Cells. We next investigated whether this would affect the formation of ectopic lymphoid tissue known to form in the meninges after transfer of $2D2^{tg}$ Th17 cells (14). We, therefore, quantified a predefined panel of cytokines in the CSF from wt-R and Bcl6KO-R (Dataset S22). The concentrations of CXCL13, CXCL16, CCL5, and CCL17 were significantly lower in Bcl6KO-R than in wt-R (Fig. 4 *A* and *B* and *SI Appendix*, Fig. S6*F*). Notably, CXCL13 increases in the CSF in MS (33) and attracts B cells by binding to CXCR5 (34), and CXCL13 and CXCL16 are known to be expressed by stromal cells, including fibroblastic reticular cells (FRCs) and follicular dendritic cells (FDCs) (34). Both *Cxcr5* and *Cxcr6*, the receptors of CXCL13 and CXCL16, were expressed by meningeal B cells and T cells in our dataset (Fig. 4*C* and *SI Appendix*, Fig. S6*G*) suggesting a potential intercellular signaling mechanism affected by Bcl6 in Th17 cells. Of note, FRCs or FDCs both constitute nonhematopoietic (i.e., $CD45^{neg}$) stromal cell types (35) and were thus not included in our $CD45^{high}$-restricted scRNA-seq screen.

We, therefore, employed surrogate markers of FRC abundance by costaining for ER-TR7, a microfibrillar protein secreted by FRCs (36), and CXCL13 in SC sections collected at the peak of AT-EAE. This revealed the presence of CXCL13 in the vicinity of B cell aggregations that also contained donor-derived $V\beta11^{+}$ T cells in the meninges of wt-R (Fig. 4*D* and *SI Appendix*, Fig. S8*A*). In accordance with a previous study (37), we did not identify $CD35^{+}$ FDCs in the meningeal B cell aggregations. ER-TR7 staining, which is secreted by FRCs (38, 39), was sparse in the meninges of Bcl6KO-R with few, small, or no B cell aggregations detected (Fig. 4*E*) in contrast to abundant ER-TR7 staining in wt-R (Fig. 4*E*). As Bcl6 expression in Th17 cells affects IL-17 secretion in vivo (Fig. 2 *C* and *I*), which has been shown by others to promote FRC formation (36), a similar mechanism may control meningeal inflammation. This suggests that Bcl6-expressing Th17 cells may modulate the meningeal microenvironment that promotes interactions between Th17 cells and B cells thereby affecting autoimmune CNS tissue damage.

Discussion

We here demonstrate that the CNS infiltration induced by AT of myelin-reactive $2D2^{tg}$ Th17 cells was highly compartmentalized between meninges and parenchyma with distinct meningeal and parenchymal phenotypes. B cells showed strong meningeal enrichment and colocalized with densely packed donor-derived Th17 cells that acquired a B cell–supporting phenotype specifically at this site. Accordingly, meningeal B cells exhibited a $CD23^{+}$ follicular rather than germinal center phenotype corresponding to a follicular helper-like phenotype of the invading Th17 cells. The lymphoid tissue-supporting and B cell–supporting function of meningeal Th17 cells was dependent on the transcription factor Bcl6 in vivo.

Our findings may have relevance for human MS. In fact, class-switched and affinity-matured Ig and late B lineage cells accumulate in the CSF in MS (7, 8) and facilitate its diagnosis (1, 2). Several studies have also shown that B cell–rich ectopic lymphoid tissue can develop in the meninges and correlate with disability in chronic MS (4, 9). It has been speculated that a gradient of neuronal damage originates from the meninges and is inflicted by soluble mediators released from the meninges like antibodies (10, 11). In such a mechanistic model, Bcl6-expressing Th17 cells would be central for controlling B cell aggregations in the meningeal compartment and, thus, disease severity.

Why is inflammation so different between the parenchyma and the meninges? We speculate that the presence of stromal cells which is unique to the meninges allows formation of lymphoid structures. We also extended previous studies that identified meningeal B cells as antigen-presenting cells (15, 40) and that reported a role of CXCL13 in Th17-mediated EAE (40) by identifying Bcl6-dependent functions in Th17 cells in the meninges. Notably, the transcription factor Bcl6 was previously identified as lineage defining for TFH cells and required for their B cell supporting function (16). Bcl6 generally functions as a transcriptional repressor inhibiting non-TFH transcriptional programs in T cells (16). Chromatin binding of Bcl6 varies considerably between B cells, TFH cells, and macrophages, which is explained by interactions with other transcriptional regulators (18, 41). This supports that Bcl6 regulates transcription in a cell type–specific manner. Whether Bcl6 effects vary between TFH and Th17 cells has not been tested. We provide evidence that Bcl6 partially controls Th17 function in vivo, albeit not their differentiation in vitro (17, 19, 20). We speculate that Th17 cells acquire a TFH-like function in vivo, because they are known to acquire Bcl6 expression after transfer (14).

We demonstrate location-specific heterogeneity of Th17 cells, which are known to acquire heterogeneous phenotypes depending on environmental clues. For example, Th17 cells can become pathogenic or nonpathogenic depending on in vitro conditions (42). Also, Th17 cells sorted ex vivo based on current IL-17 production from CNS versus lymph nodes (43) or based on previous IL-17 production from gut versus CNS (44, 45) are phenotypically and functionally diverse. Our findings identify a location-specific transcriptional phenotype of Th17 cells by identifying myelin-reactive cells through their $2D2^{tg}$ TCR. This differs from previous fate-reporting experiments that were performed with immunization-induced polyclonal Th17 cells and not with TCR-defined Th17 cells identified by TCR tracing. Tracking individual TCRs, thus, provides a different angle toward T cell stability than cytokine-based fate labeling.

We acknowledge that our experiments do not exclude a trafficking-related mechanism to account for the phenotype induced by Bcl6 deficiency. Taken together with the data from others (36), we hypothesize that the transcription factor Bcl6 promotes expression of Lymphotoxin-α and IL-17 in reactivated meningeal Th17 cells, which is required for the production of B cell–supporting CXCL13 by meningeal stromal cells (36) (*SI Appendix*, Fig. S8*B*). This attracts B cells to meningeal ectopic lymphoid tissue where they acquire a follicular phenotype and undergo antibody class switching.

By identifying a mechanism controlling local Th17/B cell interaction, our findings also lend further support to immune-related functions of the meninges. In fact, meningeal leukocytes respond to EAE (24), meningeal lymphatic vessels contribute to the disease (46), and dural sinus-associated meningeal antigen-presenting cells present CSF-derived antigens (47). We speculate that Bcl6 in invading myelin-reactive T cells controls their interaction with B cells while they traffic from the meninges to the parenchyma (48). This mechanism likely also contributes to human MS by controlling meningeal B cell maturation and class switching detected in the CSF (7) and in meningeal ectopic lymphoid tissue in chronic MS (4). It remains to be investigated whether T cell–derived Bcl6 also controls meningeal IgA^{+} PC described recently (49). In summary, this improves our understanding of the immune cell signaling in border compartments of the CNS.

Materials and Methods

Mice and AT-EAE. C57BL/6J, $CD4^{Cre}$ (50), $2D2^{tg}$ (21), $Bcl6^{fl/fl}$ (19), and TH [=IgH^{MOG} (51)] mice were used. $CD4^{Cre}Bcl6^{fl/fl}2D2^{tg}$ and $CD4^{Cre}Bcl6^{fl/fl}$ strains were bred as described (17). For AT-EAE induction (52), naïve $CD44^{low}CD62L^{high}CD4^{+}$ T cells were sorted from $2D2^{tg}$ donor mice and cultured for 2 d (2×10^6 cells/mL) with irradiated antigen-presenting cells, anti-CD3 antibody (2.5 μg/mL), IL-6 (20 ng/mL), TGF-β1 (10 ng/mL), and anti–IFN-γ antibody (10 μg/mL). Cells were split and cultured with IL-23 (10 ng/mL) for 3 d. Cells (2×10^6 cells/mL) were plated on anti-CD3 (2 μg/mL) with soluble anti-CD28 antibody (2 μg/mL) without any cytokines for 2 d. A total of 5×10^6 cells were iv injected into C57BL/6 recipients. Recipient mice were monitored daily; an ataxia score (53) was calculated (17).

Leukocyte Isolation from CNS. Blood leukocytes were labeled by iv injection of fluorescence coupled anti-CD45.2 antibody (3 μg/mouse) (22). After 5 min, animals were intracardially perfused. SC parenchyma was flushed out from the spinal canal with hydrostatic pressure. SC meninges remained attached to the vertebrae and were peeled off. SC parenchyma was cut up, digested (20 min, 37 °C) with collagenase D (2.5 mg/mL) and DNase I (0.05 mg/mL), and leukocytes were isolated with a 70/37% Percoll gradient (17). Meninges were digested under shaking (45 min, 37 °C) with 1 mg/mL collagenase D. Single cells were stained for flow cytometry. Tissue-resident viable $CD45^{high}$ $CD45iv^{neg}$ leukocytes were sorted for scRNA-seq or bulk RNA-seq ($V\beta11^{+}$ $CD4^{+}$ T cells).

Flow Cytometry and Fluorescence Activated Cell Sorting (FACS). Cells were stained with anti-mouse antibodies against CD45, CD3, CD4, TCR Vβ11, CD19, and CD11b; live/dead staining was performed with "Zombie NIR." To quantify cytokine production, cells were restimulated for 4 h with PMA, ionomycin, GolgiStop, and GolgiPlug; IL17A and IFN-γ were stained intracellularly. Cells were acquired using a Gallios (Beckman Coulter) flow cytometer or a FACSCelesta flow cytometer (Becton Dickinson), or sorted on a BD FACS Aria III. Data were analyzed using FlowJo v10.7.0_CL.

scRNA-Seq. scRNA-seq was performed with the Chromium Single Cell 3′ Kit with version 3 chemistry (10x Genomics). To avoid batch effects, all samples were processed on the same day with the same chip. Complementary DNA (cDNA) was partly used in scTCR-seq. Sequencing was done commercially on an Illumina Novaseq with 150-8-8-150 read setup. Processing of sequencing data was performed with the cellranger pipeline version 3.0.2. Unbiased cell-type clustering was performed in the four samples combined. Downstream analysis was performed with R package Seurat version 3.1.1 (54) using R version 3.6.1 (55). Further doublet depletion was done by R package DoubletDecon version 1.1.4 (56). Data were normalized and regressed to cell cycle phase score using SCTransform (57). Dimensionality reduction was done by Uniform Manifold Approximation and Projection. Clusters (and DE genes) were identified with "FindNeighbors" and "FindClusters" functions in Seurat. For cluster annotation, DE genes were searched in literature and plotted in feature plots. Details in *SI Appendix, Supplementary Methods* and Dataset S1.

Bulk RNA-Seq. RNA of flow sorted $V\beta11^{+}CD4^{+}$ T cells was purified using Quick-RNA Microprep Kit (Zymo Research). cDNA was prepared for bulk RNA-seq with a modified version of the SmartSeq2 protocol (58) and partly used for qPCR. Library preparation was done by the Next Ultra II FS DNA Library Prep Kit (New England Biolabs). Sequencing was carried out on a NextSeq500 (High-Out 75 cycle kit [Illumina]; 0-8-8-75 set up). Bulk RNA-seq analysis is described in *SI Appendix, Supplementary Methods*.

qPCR. qPCR was performed for murine TaqMan probes *Bcl6*, *Lta*, *Ltb*, and *Il17a*. Gapdh was used as a housekeeping gene.

Collection of CSF and Proteomics. Mice were anesthetized, hair was removed, and the head was mounted in a stereotaxic apparatus via ear bars. The cisterna magna was exposed under a dissecting binocular microscope (59) and punctured with a Hamilton syringe. CSF was collected by pulling the piston back carefully. Chemokines were detected with the Bio-Plex Pro mouse chemokine panel 31-plex (Bio-Rad Laboratories), and Ig isotypes were quantified using the ThermoFisher (Invitrogen) Antibody Isotyping 7-Plex Mouse ProcartaPlex Panel. Results were analyzed by the Luminex FLEXMAP 3D platform (15).

Immunofluorescence Staining. Mice were perfused with phosphate-buffered saline (PBS) and subsequently 4% paraformaldehyde (PFA). SC was dissected together with surrounding bones. Tissue was fixed in 4% PFA, decalcified in 0.3 M EDTA, and cryoprotected with 30% sucrose. Cross-sections were cut at cervical, thoracic, and lumbar levels. After tissue blocking, primary antibodies CD3, TCR Vβ11, B220, and F4/80 and secondary fluorescently labeled antibodies were used for stainings. Nuclei were visualized with DAPI staining. For intracellular Ki67 staining, cross-sections were permeabilized with 0.1% Triton before antibody staining. To quantify cell infiltration, the compartment area (parenchyma or meninges) and infiltrated area ($B220^{+}$ and $F4/80^{+}$ cells) were measured from overview images or the infiltrated cell number ($CD3^{+}$, $V\beta11^{+}CD3^{+}$, and $Ki67^{+}B220^{+}$ cells) was counted manually. Percentage infiltrated area was calculated relative to the total area of the compartment (meninges or parenchyma). The density of infiltrated cells was determined by dividing the counted cell number/area by the compartment area. Infiltrated cells were mapped in schematic heatmaps of the SC using Adobe Illustrator CS6. Heatmaps of individual mice were overlaid, and opacity of infiltrates was adapted to the number of mice [formula: $(100\%/n) \times 4$].

In some cases, isolated SC parenchyma enveloped in meninges were immediately frozen in Tissue-Tek. Longitudinal sections were fixed in −20 °C methanol, blocked in 1% bovine serum albumin (BSA) in PBS, and stained for B220, TCR Vβ11, CD4, CD45.2, Laminin-111 "pan laminin" (60), CXCL13, or ER-TR7. Staining was otherwise as above. Sections were examined using a Zeiss AxioImager and acquired images analyzed using Volocity 6.3 (PerkinElmer) software. Overview images were acquired with a Zeiss LSM700 confocal microscope, and images were analyzed using ZEN gray/blue (Zeiss) software. Details for immunofluorescence staining in *SI Appendix, Supplementary Methods*.

In Vitro Th17 Polarization and Proliferation of $CD4^{+}$ T Cells Isolated from EAE Mice. Active EAE was induced by subcutaneous injection of $MOG_{35–55}$ peptide (200 μg/mouse) and *Mycobacterium tuberculosis* H37Ra extract (1 mg/mL, BD) emulsified in complete Freund's adjuvant (200 μl/mouse). $CD4^{+}$ T cells and $CD11c^{+}$ DCs were isolated from draining lymph nodes and spleen on day 10 after active $MOG_{35–55}$ EAE induction using magnetic beads (Miltenyi Biotec). $CD4^{+}$ T cells and $CD11c^{+}$ DCs were cocultured in a 5:1 ratio in the presence of $MOG_{35–55}$ (20 μg/mL) and coated anti-CD3 (0.5 μg/mL). For proliferation assays, $CD4^{+}$ T cells were additionally stained with CellTrace Violet (Thermo Fisher), and T cell proliferation was analyzed by flow cytometry. For Th17 polarization, TGF-β1 (10 ng/mL), IL-6 (20 ng/mL), and anti–IFN-γ (10 μg/mL) was added to the culture, and intracellular cytokines were analyzed after 4 d by flow cytometry.

In Vitro B Cell Proliferation. MOG-specific $CD19^{+}$ B cells were isolated with MicroBeads (Miltenyi Biotec) from spleen and iLN of a naïve TH mouse [synonymously IgH^{MOG} mice (51)] and labeled with cell proliferation dye CellTrace Violet (Thermo Fisher). Labeled B cells were cocultured in a 2:1 ratio with in vitro differentiated Th17 cells from $2D2^{tg}$ mice in the presence of $MOG_{35–55}$ peptide (3 μg/mL). Th17 had been differentiated as in AT-EAE (see in *Mice and AT-EAE*). On day 3, B cell proliferation was analyzed by flow cytometry.

Statistics. Data are presented as combined box-and-whisker/dot plots (median, 25th to 75th percentiles, 1.5-fold interquartile range). Dots illustrate individual values. Data were compared using Student's *t* test for normally distributed datasets, otherwise Mann–Whitney *U* test was applied. *P* value < 0.05 was considered significant. GraphPad Prism 5 was used for statistical analysis. Statistical analyses of sequencing data were done in R.

Data Availability. The raw sequencing data supporting the findings in this study have been deposited in the Gene Expression Omnibus (GEO) repository under accession code GSE178085 (61). For sequencing analyses, we followed official tutorials and did not use any custom specific code. All processed sequencing data are included among the Datasets S1–S26. A full overview of the methods is provided in *SI Appendix, Supplementary Methods*. Previously published data were used for this work (we reproduced *SI Appendix*, Fig. S5 *A–C* from ref. 17).

ACKNOWLEDGMENTS. We thank Carolin Lewe and Sophie Loismann for excellent technical support. This work was supported by grants from the Deutsche Forschungsgemeinschaft (DFG) to G.M.z.H. (ME4050/4-1, ME4050/12-1) and to L.S. (TR128 B03; SFB1009 A02, EXC1009). G.M.z.H. was supported by the Heisenberg program of the DFG (ME4050/13-1) by DFG Grant ME4050/8-1 under the frame of E-Rare-3, the European Research Area (ERA)-Net for Research on Rare Diseases, the Grant for Multiple Sclerosis Innovation (Merck), and by a grant from the Ministerium für Innovation, Wissenschaft und Forschung des Landes Nordrhein-Westfalen. M. Heming and G.M.z.H. were supported by the Interdisciplinary Center for Clinical Research of the medical faculty of Münster (Grant MzH3/020/20 to G.M.z.H. and SEED/016/21 to

M. Heming). This work was supported, in part, by the Andrew M. and Jane M. Bursky Center for Human Immunology and Immunotherapy Programs at Washington University, Immunomonitoring Laboratory (to G.F.W.). G.F.W. was supported by grant funding from the NIH (R01 NS106289) and the National Multiple Sclerosis Society (NMSS; RG-1802-30253). A.P. was supported by grant funding from Emmy Noether (PE2681/1-1).

1. M. Filippi *et al*., Multiple sclerosis. *Nat. Rev. Dis. Primers* **4**, 43 (2018).
2. D. S. Reich, C. F. Lucchinetti, P. A. Calabresi, Multiple sclerosis. *N. Engl. J. Med.* **378**, 169–180 (2018).
3. J. Machado-Santos *et al*., The compartmentalized inflammatory response in the multiple sclerosis brain is composed of tissue-resident CD8+ T lymphocytes and B cells. *Brain* **141**, 2066–2082 (2018).
4. B. Serafini, B. Rosicarelli, R. Magliozzi, E. Stigliano, F. Aloisi, Detection of ectopic B-cell follicles with germinal centers in the meninges of patients with secondary progressive multiple sclerosis. *Brain Pathol.* **14**, 164–174 (2004).
5. B. Engelhardt, P. Vajkoczy, R. O. Weller, The movers and shapers in immune privilege of the CNS. *Nat. Immunol.* **18**, 123–131 (2017).
6. K. Alves de Lima, J. Rustenhoven, J. Kipnis, Meningeal immunity and its function in maintenance of the central nervous system in health and disease. *Annu. Rev. Immunol.* **38**, 597–620 (2020).
7. S. Cepok *et al*., Short-lived plasma blasts are the main B cell effector subset during the course of multiple sclerosis. *Brain* **128**, 1667–1676 (2005).
8. A. Palanichamy *et al*., Immunoglobulin class-switched B cells form an active immune axis between CNS and periphery in multiple sclerosis. *Sci. Transl. Med.* **6**, 248ra106 (2014).
9. M. Calabrese *et al*., Cortical lesion load associates with progression of disability in multiple sclerosis. *Brain* **135**, 2952–2961 (2012).
10. R. Magliozzi *et al*., A gradient of neuronal loss and meningeal inflammation in multiple sclerosis. *Ann. Neurol.* **68**, 477–493 (2010).
11. L. Schirmer *et al*., Neuronal vulnerability and multilineage diversity in multiple sclerosis. *Nature* **573**, 75–82 (2019).
12. M. Rangachari, V. K. Kuchroo, Using EAE to better understand principles of immune function and autoimmune pathology. *J. Autoimmun.* **45**, 31–39 (2013).
13. A. Jäger, V. Dardalhon, R. A. Sobel, E. Bettelli, V. K. Kuchroo, Th1, Th17, and Th9 effector cells induce experimental autoimmune encephalomyelitis with different pathological phenotypes. *J. Immunol.* **183**, 7169–7177 (2009).
14. A. Peters *et al*., Th17 cells induce ectopic lymphoid follicles in central nervous system tissue inflammation. *Immunity* **35**, 986–996 (2011).
15. C. R. Parker Harp *et al*., Neutrophils promote VLA-4-dependent B cell antigen presentation and accumulation within the meninges during neuroinflammation. *Proc. Natl. Acad. Sci. U.S.A.* **116**, 24221–24230 (2019).
16. R. I. Nurieva *et al*., Bcl6 mediates the development of T follicular helper cells. *Science* **325**, 1001–1005 (2009).
17. D. Schafflick *et al*., Integrated single cell analysis of blood and cerebrospinal fluid leukocytes in multiple sclerosis. *Nat. Commun.* **11**, 247 (2020).
18. K. Hatzi *et al*., BCL6 orchestrates Tfh cell differentiation via multiple distinct mechanisms. *J. Exp. Med.* **212**, 539–553 (2015).
19. K. Hollister *et al*., Insights into the role of Bcl6 in follicular Th cells using a new conditional mutant mouse model. *J. Immunol.* **191**, 3705–3711 (2013).
20. A. Mondal, D. Sawant, A. L. Dent, Transcriptional repressor BCL6 controls Th17 responses by controlling gene expression in both T cells and macrophages. *J. Immunol.* **184**, 4123–4132 (2010).
21. E. Bettelli *et al*., Myelin oligodendrocyte glycoprotein-specific T cell receptor transgenic mice develop spontaneous autoimmune optic neuritis. *J. Exp. Med.* **197**, 1073–1081 (2003).
22. E. M. Steinert *et al*., Quantifying memory CD8 T cells reveals regionalization of immunosurveillance. *Cell* **161**, 737–749 (2015).
23. D. Schafflick *et al*., Single-cell profiling of CNS border compartment leukocytes reveals that B cells and their progenitors reside in non-diseased meninges. *Nat. Neurosci.*, 10.1038/s41593-021-00880-y (2021).
24. M. J. C. Jordão *et al*., Single-cell profiling identifies myeloid cell subsets with distinct fates during neuroinflammation. *Science* **363**, eaat7554 (2019).
25. M. Heming *et al*., Neurological manifestations of COVID-19 feature T cell exhaustion and dedifferentiated monocytes in cerebrospinal fluid. *Immunity* **54**, 164–175.e6 (2021).
26. V. Schropp *et al*., Contribution of LTi and T_H17 cells to B cell aggregate formation in the central nervous system in a mouse model of multiple sclerosis. *J. Neuroinflammation* **16**, 111 (2019).
27. M. P. Mycko *et al*., A heat shock protein gene (Hsp70.1) is critically involved in the generation of the immune response to myelin antigen. *Eur. J. Immunol.* **38**, 1999–2013 (2008).
28. Q.-H. Meng, H. N. White, $CD21^{int}$ $CD23^{+}$ follicular B cells express antigen-specific secretory IgM mRNA as primary and memory responses. *Immunology* **151**, 211–218 (2017).
29. B. Knier *et al*., Myeloid-derived suppressor cells control B cell accumulation in the central nervous system during autoimmunity. *Nat. Immunol.* **19**, 1341–1351 (2018).
30. L. Rijvers *et al*., The macrophage migration inhibitory factor pathway in human B cells is tightly controlled and dysregulated in multiple sclerosis. *Eur. J. Immunol.* **48**, 1861–1871 (2018).
31. G. M. Cox *et al*., Macrophage migration inhibitory factor potentiates autoimmune-mediated neuroinflammation. *J. Immunol.* **191**, 1043–1054 (2013).
32. M. Mitsdoerffer *et al*., Proinflammatory T helper type 17 cells are effective B-cell helpers. *Proc. Natl. Acad. Sci. U.S.A.* **107**, 14292–14297 (2010).
33. M. Krumbholz *et al*., Chemokines in multiple sclerosis: CXCL12 and CXCL13 up-regulation is differentially linked to CNS immune cell recruitment. *Brain* **129**, 200–211 (2006).
34. A. E. Denton *et al*., Type I interferon induces CXCL13 to support ectopic germinal center formation. *J. Exp. Med.* **216**, 621–637 (2019).
35. N. J. Krautler *et al*., Follicular dendritic cells emerge from ubiquitous perivascular precursors. *Cell* **150**, 194–206 (2012).
36. N. B. Pikor *et al*., Integration of Th17- and lymphotoxin-derived signals initiates meningeal-resident stromal cell remodeling to propagate neuroinflammation. *Immunity* **43**, 1160–1173 (2015).
37. A. K. Dang, Y. Tesfagiorgis, R. W. Jain, H. C. Craig, S. M. Kerfoot, Meningeal infiltration of the spinal cord by non-classically activated B cells is associated with chronic disease course in a spontaneous B cell-dependent model of CNS autoimmune disease. *Front. Immunol.* **6**, 470 (2015).
38. M. Sixt *et al*., The conduit system transports soluble antigens from the afferent lymph to resident dendritic cells in the T cell area of the lymph node. *Immunity* **22**, 19–29 (2005).
39. E. Van Vliet, M. Melis, J. M. Foidart, W. Van Ewijk, Reticular fibroblasts in peripheral lymphoid organs identified by a monoclonal antibody. *J. Histochem. Cytochem.* **34**, 883–890 (1986).
40. J. L. Quinn, G. Kumar, A. Agasing, R. M. Ko, R. C. Axtell, Role of TFH cells in promoting T helper 17-induced neuroinflammation. *Front. Immunol.* **9**, 382 (2018).
41. X. Liu *et al*., Genome-wide analysis identifies Bcl6-controlled regulatory networks during T follicular helper cell differentiation. *Cell Rep.* **14**, 1735–1747 (2016).
42. Y. Lee *et al*., Induction and molecular signature of pathogenic TH17 cells. *Nat. Immunol.* **13**, 991–999 (2012).
43. J. T. Gaublomme *et al*., Single-cell genomics unveils critical regulators of Th17 cell pathogenicity. *Cell* **163**, 1400–1412 (2015).
44. N. Gagliani *et al*., Th17 cells transdifferentiate into regulatory T cells during resolution of inflammation. *Nature* **523**, 221–225 (2015).
45. K. Hirota *et al*., Fate mapping of IL-17-producing T cells in inflammatory responses. *Nat. Immunol.* **12**, 255–263 (2011).
46. A. Louveau *et al*., CNS lymphatic drainage and neuroinflammation are regulated by meningeal lymphatic vasculature. *Nat. Neurosci.* **21**, 1380–1391 (2018).
47. J. Rustenhoven *et al*., Functional characterization of the dural sinuses as a neuroimmune interface. *Cell* **184**, 1000–1016.e27 (2021).
48. C. Schläger *et al*., Effector T-cell trafficking between the leptomeninges and the cerebrospinal fluid. *Nature* **530**, 349–353 (2016).
49. O. L. Rojas *et al*., Recirculating intestinal IgA-producing cells regulate neuroinflammation via IL-10. *Cell* **176**, 610–624.e18 (2019).
50. P. P. Lee *et al*., A critical role for Dnmt1 and DNA methylation in T cell development, function, and survival. *Immunity* **15**, 763–774 (2001).
51. T. Litzenburger *et al*., B lymphocytes producing demyelinating autoantibodies: Development and function in gene-targeted transgenic mice. *J. Exp. Med.* **188**, 169–180 (1998).
52. G. Meyer Zu Horste *et al*., Fas promotes T helper 17 cell differentiation and inhibits T helper 1 cell development by binding and sequestering transcription factor STAT1. *Immunity* **48**, 556–569.e7 (2018).
53. S. J. Guyenet *et al*., A simple composite phenotype scoring system for evaluating mouse models of cerebellar ataxia. *J. Vis. Exp.* **39**, 1787 (2010).
54. T. Stuart *et al*., Comprehensive integration of single-cell data. *Cell* **177**, 1888–1902.e21 (2019).
55. J. Wolbert *et al*., Redefining the heterogeneity of peripheral nerve cells in health and autoimmunity. *Proc. Natl. Acad. Sci. U.S.A.* **117**, 9466–9476 (2020).
56. E. A. K. DePasquale *et al*., DoubletDecon: Deconvoluting doublets from single-cell RNA-sequencing data. *Cell Rep.* **29**, 1718–1727.e8 (2019).
57. C. Hafemeister, R. Satija, Normalization and variance stabilization of single-cell RNA-seq data using regularized negative binomial regression. *Genome Biol.* **20**, 296 (2019).
58. S. Picelli *et al*., Smart-seq2 for sensitive full-length transcriptome profiling in single cells. *Nat. Methods* **10**, 1096–1098 (2013).
59. V. Narayanan *et al*., Impairment of frequency-specific responses associated with altered electrical activity patterns in auditory thalamus following focal and general demyelination. *Exp. Neurol.* **309**, 54–66 (2018).
60. L. M. Sorokin *et al*., Developmental regulation of the laminin α5 chain suggests a role in epithelial and endothelial cell maturation. *Dev. Biol.* **189**, 285–300 (1997).
61. M. Hartlehnert *et al*., Bcl6 controls meningeal Th17-B cell interaction in murine neuroinflammation. *Gene Expression Omnibus*. https://www.ncbi.nlm.nih.gov/geo/query/acc.cgi?acc=GSE178085. Deposited 14 June 2021.